Monthly Notices
of the
ROYAL ASTRONOMICAL SOCIETY

MNRAS **462,** 1735–1748 (2016)
Advance Access publication 2016 July 25

doi:10.1093/mnras/stw1682

94 Ceti: a triple star with a planet and dust disc★,†

J. Wiegert,[1]‡ V. Faramaz[2] and F. Cruz-Saenz de Miera[3]

[1]*Department of Earth and Space Sciences, Chalmers University of Technology, Onsala Space Observatory, SE-439 92 Onsala, Sweden*
[2]*Instituto de Astrofísica, Pontificia Universidad Católica de Chile, Vicuña Mackenna 4860, 7820436 Macul, Santiago, Chile*
[3]*Instituto Nacional de Astrofísica, Optica y Electrónica, Luis Enrique Erro 1, Tonantzintla, Puebla, 72840, México*

Accepted 2016 July 11. Received 2016 July 9; in original form 2016 April 26

ABSTRACT

94 Ceti is a triple star system with a circumprimary gas giant planet and far-infrared excess. Such excesses around main sequence stars are likely due to debris discs, and are considered as signposts of planetary systems and, therefore, provide important insights into the configuration and evolution of the planetary system. Consequently, to learn more about the 94 Ceti system, we aim to model the dust emission precisely to fit its observed spectral energy distribution and to simulate its orbital dynamics. We interpret our APEX bolometric observations and complement them with archived *Spitzer* and *Herschel* bolometric data to explore the stellar excess and to map out background sources in the fields. Dynamical simulations and 3D radiative transfer calculations were used to constrain the debris disc configurations and model the dust emission. The best-fitting dust disc model for 94 Ceti implies a circumbinary disc around the secondary pair, limited by dynamics to radii smaller than 40 au and with a grain-size power-law distribution of $\sim a^{-3.5}$. This model exhibits a dust-to-star luminosity ratio of $4.6 \pm 0.4 \times 10^{-6}$. The system is dynamically stable and *N*-body symplectic simulation results are consistent with semi-analytical equations that describe orbits in binary systems. In the observations, we also find tentative evidence of a circumtertiary ring that could be edge-on.

Key words: binaries: general – stars: individual: 94 Ceti (HD 19994, HIP 14954) – planetary systems – infrared: stars – submillimetre: stars.

1 INTRODUCTION

Approximately half of the stars belong to binary or multiple systems (Duquennoy & Mayor 1991; Lada 2006; Eggleton & Tokovinin 2008; Raghavan et al. 2010; Duchêne & Kraus 2013). Stellar companions may have a large impact on planetary formation processes. In particular, they are found to truncate circumstellar discs and put a limit on the extent of material available for planetary formation (Artymowicz & Lubow 1994; Jang-Condell, Mugrauer & Schmidt 2008; Andrews et al. 2010; Jang-Condell 2015). They are also expected to stir and increase the eccentricities and relative velocities of planetesimals and planetary embryos that might have formed around the primary (Quintana et al. 2007; Thébault, Marzari & Scholl 2009; Rafikov & Silsbee 2015). Consequently, multiple star systems generate significant collisional activity, which may shorten the lifetime of a disc and make it difficult to form planets. Observations tend to support this, since it was found that protoplanetary discs are half as common in young (a few million years) binary stars compared to single stars (Cieza et al. 2009; Kraus et al. 2012). In addition, these discs are much less massive compared to those found around single stars (by a factor ∼5–25, Harris et al. 2012) and were found to be more short-lived as well (Duchêne 2010).

However, debris discs have been found around old binary stars, first with *Spitzer* (Trilling et al. 2007) and then with *Herschel* (Rodriguez et al. 2015). They were detected through their host star infrared (IR) excess emission, a signature of the presence of micron-sized dust grains. These grains are expected to acquire unstable orbits due to both gravitational and non-gravitational perturbations. The latter scenario includes radiation pressure and Poynting–Robertson drag, which effectively clear dust clouds of small and large grains (<1 μm and between 1 μm to 1 mm, respectively). As such, dust in circumstellar discs must be continuously replenished from collisional processes in rings of parent bodies (planetesimals) akin to that of the asteroid and Edgeworth–Kuiper belts in our Solar system (Artymowicz 1997; Krivov et al. 2008; Wyatt 2008; Moro-Martin 2013). These underlying reservoirs of large bodies

★This publication is based on observations with *Herschel*, which is an ESA space observatory with science instruments provided by the European-led principal investigator consortia and with important participation from NASA.

†It is also based on data acquired with the Atacama Pathfinder Experiment (APEX), which is a collaboration between the Max-Planck-Institut für Radioastronomie, the European Southern Observatory and the Onsala Space Observatory.

‡E-mail: joachim.wiegert@chalmers.se

show that the presence of a stellar companion does not necessarily hinder the formation of the building blocks necessary to form planets.

The presence of at least one stellar companion does not necessarily inhibit planetary formation either, since numerous planets have been found in binary or multiple systems. However, the majority of these planets were found in wide binary systems (Mugrauer et al. 2005; Daemgen et al. 2009; Muterspaugh et al. 2010; Bergfors et al. 2013). When the companion is not expected to affect planetary formation processes significantly, it is not surprising that these systems are found to be hosts to planets (Eggenberger et al. 2007; Desidera & Barbieri 2007; Duchêne 2010) and that the properties of circumstellar protoplanetary and debris discs in binaries are found to be similar to those hosted by single stars for separations larger than several tens of astronomical units (Kraus et al. 2012; Harris et al. 2012; Rodriguez et al. 2015).

According to the Open Exoplanet Catalogue[1] (during the summer of 2016), out of the 130 multiple star systems with planets, only less than one-fifth (23) are triple star systems. This is expected considering that triple star systems represent less than one-fifth of the multiple star systems (Raghavan et al. 2010). In most triple star systems, the planet is orbiting the primary star with a secondary stellar binary surrounding the primary on a wider orbit.

In addition, investigating associated debris discs and tracing the interactions between discs, planets and/or stellar companions can considerably aid our understanding of the dynamical history of a planetary system. This kind of study was carried out for the Solar system with the Nice model of Gomes et al. (2005), but also for the systems of e.g. β Pictoris (see e.g. Dent et al. 2014; Nesvold & Kuchner 2015; Millar-Blanchaer et al. 2015; Apai et al. 2015), Fomalhaut (see e.g. Beust et al. 2014; Faramaz et al. 2015; Cataldi et al. 2015; Lawler, Greenstreet & Gladman 2015), HR 8799 (see e.g. Moore & Quillen 2013; Contro et al. 2015; Booth et al. 2016), τ Ceti (Lawler et al. 2014), and HD 69830 (Payne et al. 2009). Therefore, studying in detail close binary or hierarchical systems, where both planets and circumstellar emission have been found, is crucial.

Five systems, out of the 23 found in triple star systems mentioned above, are associated with circumstellar dust emission. These are HD 178911 (Saffe & Gómez 2004; Kóspál et al. 2009), Fomalhaut (Aumann 1985; Kalas et al. 2008; Mamajek et al. 2013; Su et al. 2016), HD 40979 (e.g. Kóspál et al. 2009; Dodson-Robinson et al. 2011), 51 Eridani (e.g. Riviere-Marichalar et al. 2014), and 94 Ceti (HIP 14954, HD 19994). Another possible candidate is L1551 IRS 5, which is a young embedded binary system and potentially a triple star system (Lim & Takakuwa 2006). Due to the low number of known triple star systems with both planets and dust emission, it is important to study each of these in great detail. We will focus here on the 94 Cet system.

The third star of 94 Cet was recently discovered by Röll et al. (2011, 2012) with astrometry, speckle interferometry and radial velocity measurements. The system is associated with at least one circumprimary planet (Eggenberger, Udry & Mayor 2003), and also shows a far-infrared (FIR) excess emission (Trilling et al. 2008; Eiroa et al. 2013) that possibly originates from circumstellar dust. This is a hierarchical triple star system, at a distance of 22.6 $\pm$ 0.1 pc from the Sun, where 94 Cet A is an F8 V star, and 94 Cet B and C are both M dwarfs that form a binary pair, which together orbits the primary on a 2029-year-long orbit.

[1] http://www.openexoplanetcatalogue.com/ (Rein 2012).

The IR excess of 94 Cet was detected by Trilling et al. (2008) with *Spitzer*/MIPS at 70 μm and later confirmed at 100 and 160 μm by Eiroa et al. (2013) as part of the key project DUNES (dust around nearby stars) of *Herschel* (Pilbratt et al. 2010). IR excesses at such long wavelengths originate from the thermal emission of dust particles surrounding the star. To improve the coverage of the spectral energy distribution (SED) we observed this system with APEX (the Atacama Pathfinder Experiment) at 870 μm.

Eiroa et al. (2013) found that the inferred dust temperature corresponds to a blackbody radial distance from the primary star that corresponds to a dynamical unstable region due to the companion stars. Another hint that this emission may not be associated with 94 Cet A is that there is a marginally significant offset between the expected and observed position of the source, if it is comoving with 94 Cet A. It may, thus, be a background source or be associated with the other stellar members of this system.

The structure of this paper is as follows; we present the stellar and system properties in Section 2, and we summarize the observations, data reduction and the observational results in Section 3. In Sections 4 and 5, we discuss the nature of the excess, the extended emission, and background sources. Assuming that the excesses originate from disc(s), we apply both dynamical simulations and radiative transfer simulations and present these results in Section 6, and summarize our conclusions in Section 7.

2 STELLAR AND SYSTEM PROPERTIES

The binary nature of 94 Cet was first discovered by Admiral Smyth in 1836 (Raghavan et al. 2006; Smyth 1844), who was able to resolve the stars (they share proper motion, $\mu_\alpha = 194.56 \pm 0.37$ mas yr^{-1} and $\mu_\delta = -69.01 \pm 0.30$ mas yr^{-1}). The orbital parameters have been constrained and refined by Hale (1994), and more recently by Roberts et al. (2011). The companion star is a binary with two M dwarfs on a 1-year orbit (Röll et al. 2011, 2012), which together orbits 94 Cet A on a 2029-year-long orbit. Fig. 1 shows a schematic overview of this system and the orbital parameters are summarized in Table 1.

In the CORALIE survey, which is based on radial velocity measurements, a planetary companion around the primary star was also discovered (Queloz et al. 2004; Mayor et al. 2004), designated 94 Cet Ab. This planet has a mass of $m_b \sin i = 1.7\,M_{\rm Jup}$, period of 536 d and a semi-major axis of 1.4 au.

The properties of the two companion stars are not well known, as previous works were based on the assumption that 94 Cet is a binary. However, their masses have been estimated by Röll et al. (2011, 2012) with radial velocity measurements. These masses suggest them to be M class main sequence stars (the primary star's age is between 1 and 5 Gyr) and so we may use other studies to infer additional properties. From Cox (2000, pp. 388–389) we find that the masses 0.55 $M_\odot$ and 0.34 $M_\odot$ of main sequence stars correspond to the spectral classes M0 and M3, respectively. Bessell (1991) showed that these spectral classes have effective temperatures of 3700 and 3300 K and luminosities of 0.05 $L_\odot$ and 0.01–0.015 $L_\odot$, respectively (see also Rajpurohit et al. 2013). With these data, we approximate their radii (Stefan–Boltzmann law) to 0.6 and 0.3 $R_\odot$ and estimate their surface gravity to $\log g = 4.7$ and 5.0, respectively (see Table 2).

3 OBSERVATIONAL DATA

In this work, we made use of photometric data to obtain the properties of the dust conforming to the disc surrounding 94 Cet, and

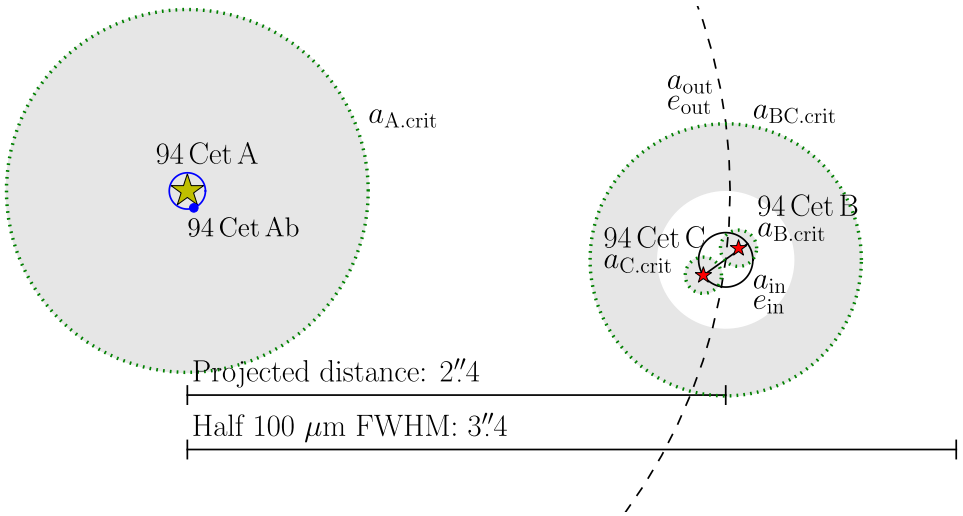

Figure 1. Schematic overview of the known components of the 94 Cet system (not to scale). The *outer orbit* denotes the orbit of the binary pair, 94 Cet BC, around 94 Cet A, where $a_{\rm out}$ is the semi-major axis (220 au) and $e_{\rm out}$ is the eccentricity (0.26). We denote the orbit of 94 Cet C around 94 Cet B as the *inner orbit* and similarly, $a_{\rm in}$ and $e_{\rm in}$ are the inner semi-major axis (0.99 au) and eccentricity (0.36). The blue dot and line indicate the orbit of the planet 94 Cet Ab with a semi-major axis of 1.42 au and eccentricity of 0.30. The green dotted lines are the critical semi-major axes. Areas where we can expect stable orbits are shown as shaded regions, which are denoted as $a_{\rm A.crit}$, $a_{\rm B.crit}$, $a_{\rm C.crit}$ and $a_{\rm BC.crit}$ ($a_{\rm ABC.crit}$ is outside this figure). The projected distance refers to the angular distance between the stars during the observations and this is compared to half of the *Herschel* beam FWHM at 100 μm.

Table 1. 94 Cet orbital parameters.

	Outer orbit[a]	Inner orbit[b]	Planetary orbit[c]
Semi-major axis (au)	220 ± 5	0.99 ± 0.02	1.42 ± 0.01
Period (yr)	2029 ± 41	1.04 ± 0.01	1.47 ± 0.01
Eccentricity	0.26 ± 0.01	0.36 ± 0.01	0.30 ± 0.04
Inclination to line of sight, i (°)	104 ± 2	108.5 ± 0.7	–
Argument of periapsis, ω (°)	342 ± 7	334.9 ± 2.3	–
Longitude of ascending node, Ω (°)	97 ± 2	190.9 ± 1.0	–

Notes. [a]Roberts et al. (2011); [b]Röll et al. (2011, 2012); [c]Mayor et al. (2004).

Table 2. Stellar properties.

Property	94 Cet A HIP 14954 A, HD 19994	94 Cet B	94 Cet C
ICRS[a] (J2000) RA	$3^{\rm h}12^{\rm m}46\overset{\rm s}{.}44$	–	–
ICRS (J2000) Dec.	$-1°11'45\overset{''}{.}96$	–	–
Spectral class	F8 V to G0 IV	M0 V[b]	M3 V[b]
Effective temperature (K)	6187	3700[c]	3300[c]
Luminosity ($L_\odot$)	3.85	0.05[c]	0.01[c]
Mass ($M_\odot$)	1.34[d]	0.55[e]	0.34[e]
Radius ($R_\odot$)	1.82 ± 0.07[f]	0.55[g]	0.31[g]
log (g)	4.24	4.7[h]	5.0[h]
Metallicity [Fe/H]	0.21	–	–
Age (Gyr)[i]	1.17–5.67	1.17–5.67	1.17–5.67
Distance (pc)	22.6 ± 0.1	22.6 ± 0.1	22.6 ± 0.1
Proper motion (mas yr^{-1}), RA	195[j]	195[j]	–
Proper motion (mas yr^{-1}), Dec.	−67[j]	−67[j]	–

Notes. General reference is Eiroa et al. (2013, and references therein) except when stated otherwise. [a]International Celestial Reference System. [b]Estimate from tables in Cox (2000, pp. 388–389) using the known dynamical mass. [c]Estimate from tables in Bessell (1991) using the spectral class. [d]Mayor et al. (2004). [e]Röll et al. (2011, 2012). [f]Fuhrmann (2008). [g]Estimate from Stefan–Boltzmann law $L \approx 4\pi R^2 \sigma T^4$. [h]Approximated from radius and mass to find a spectral model in a PHOENIX grid. [i]Age range based on both X-ray luminosities and activity index $\log R'_{\rm HK}$ (Eiroa et al. 2013). [j]94 Cet's system proper motion is $\mu_\alpha = 194.56 \pm 0.37$ mas yr^{-1} and $\mu_\delta = -69.01 \pm 0.30$ mas yr^{-1} (Eiroa et al. 2013 and SIMBAD Astronomical Database http://simbad.u-strasbg.fr/simbad/).

of imaging data used to make a spatial analysis of the whole system. In this section, we explain how we obtained and processed the *Herschel* and APEX-LABOCA data plus we present the supplementary data used in our analysis. The complete observational data are presented in Table 3.

3.1 *Herschel*

The *Herschel*/PACS (Poglitsch et al. 2010) observations were taken as part of the DUNES Open Time Key Programme and were published by Eiroa et al. (2013),[2] where a more detailed description is given (see also Montesinos et al. 2016 for further details). Scan map observations by *Herschel*/PACS were taken with the 100/160 channel combination during OD 661. The *Herschel* observations are summarized here in Table 3.

[2] The DUNES data archive can be found at http://sdc.cab.inta-csic.es/dunes/jsp/masterTableForm.jsp

3.1.1 *Data reduction*

The observations were reduced using the Herschel Interactive Processing Environment, HIPE (Ott 2010), version 13.0.0, using the PACS calibration version 69. PACS images are affected by shot noise (frequency dependent, $1/f$), consequently, we used a high-pass filter to reduce these effects. We chose radii of 20 and 25

Table 3. Observation log of data used in our analysis.

Instrument/ Mode	Obs/Pgm ID/ AORKEY	$\lambda_{\rm eff}$ (μm)	Beam FWHM (arcsec)	Observing date (yr-month-dy)	$t_{\rm int}$ [a] (s)	Field centre coordinates (J2000)	Offset[b] (arcsec)
Spitzer/MIPS	4080640	24	5.9	2005-01-23	48	$3^{\rm h}12^{\rm m}46\overset{\rm s}{.}43$, $-1°11'48\overset{''}{.}2$	2.0
	4080640	70	19	2005-01-23	440	$3^{\rm h}12^{\rm m}46\overset{\rm s}{.}51$, $-1°11'46\overset{''}{.}4$	1.8
Herschel/PACS	1342216129	100	6.8	2011-03-06	1440	$3^{\rm h}12^{\rm m}46\overset{\rm s}{.}36$, $-1°11'47\overset{''}{.}5$	5.0
	1342216130	160	11.4	2011-03-06	1440	$3^{\rm h}12^{\rm m}46\overset{\rm s}{.}36$, $-1°11'47\overset{''}{.}5$	6.2
APEX-LABOCA	090.F-9302(A)	870	19.5	2012-08-15 to 2012-11-27	28 905	$3^{\rm h}12^{\rm m}46\overset{\rm s}{.}44$, $-1°11'46\overset{''}{.}0$	–

Notes. [a] $t_{\rm int}$ is the on-source integration time. [b] Offset between measured main source position and source tabulated coordinates (J2000) of the primary star compensated for proper motion. The average offset for PACS is 2.4 arcsec (Sánchez-Portal et al. 2014) at this observing period (OD 661).

frames for 100 and 160 μm, respectively, allowing us to eliminate background structures larger than 82 and 102 arcsec. By the nature of the procedure, high-pass filtering results in a flux loss, which we rectify by masking all pixels 10 times brighter than the standard deviation of non-zero flux pixels. Deglitching was done using the second-level spatial deglitching task in HIPE. PACS observations were carried out at two different observational angles to decrease striping effects. In the final maps, we combined individual scans for each band to increase the signal-to-noise ratio (SNR). Finally, we used a drizzling method to obtain a final image scale of 1 arcsec per pixel at 100 μm and 2 arcsec per pixel at 160 μm compared to the native instrument pixel sizes of 3.2 arcsec for 100 μm and 6.4 arcsec for 160 μm.

3.1.2 *Aperture photometry*

Aperture photometry was performed using radii of 5 and 8 arcsec for 100 and 160 μm, respectively; these particular radii were used because they were found to maximize the SNR by Eiroa et al. (2013). We performed aperture and colour corrections following Balog et al. (2014). For the aperture corrections, we divided the integrated flux by 0.521 for 100 μm and by 0.527 for 160 μm. The colour corrections were done by dividing the aperture-corrected flux by 1.033 for 100 μm and 1.074 for 160 μm; these values are correct for blackbody temperatures around 5000 K (table 1 of *Herschel* documentation PICC-ME-TN-038, Müller, Okumura & Klaas 2011).

To check whether or not our source is extended, we compared the full width at half-maximum (FWHM) of 2D Gaussian fits with the beam FWHM. We found that only the central source was marginally extended, as we can see in the radial profiles shown in Fig. 2. The profile error in this plot is estimated from the standard deviation of the radial profiles to the east, west, south and north of the central source, and from the observed uncertainty. The FWHMs of Gaussians fitted on the central source were 8.2 and 10.9 arcsec at 100 and 160 μm, respectively. These correspond to 185 and 246 au at the system's distance. The point spread function (PSF) FWHM is 6.8 arcsec at 100 μm and 11.4 arcsec at 160 μm with a scan speed of 20 arcsec s^{-1}. Thus, we used an aperture with a radius of 6 arcsec at 100 μm, and the aperture correction used on the central source was 0.595 (see also Marshall et al. 2014 for details).

The integrated flux uncertainty was estimated in a process similar to the one explained in Eiroa et al. (2013). We began by measuring the fluxes inside 40 squared apertures, each with the same area as the aperture used for 94 Cet. They were put at random positions, in annuli between 10 and 20 arcsec from the source aperture, and we made sure to avoid all of the nearby sources. Subsequently, the standard deviation of all of these integrated fluxes

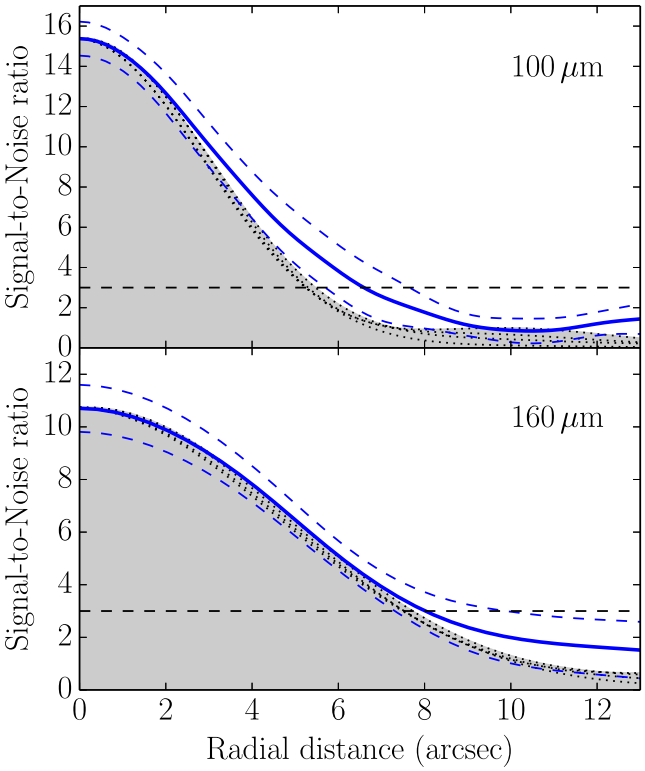

Figure 2. In blue, we show the average radial profiles of the central source (continuous) and its uncertainties (dashed) compared with profiles of the α Boö PSF plotted as grey fields and dotted black curves. The 3 × rms is indicated with the horizontal dashed black line.

was multiplied by $\sqrt{1+1/N}$, where N is the number of background squares. Lastly, for the final error estimate, we incorporated the calibration error (5 per cent, Balog et al. 2014) with a quadratic sum.

3.2 APEX-LABOCA

APEX is a 12-m millimetre/submillimetre telescope located at 5105 m altitude on the Llano de Chajnantor, Chile, with a pointing accuracy of 2 arcsec.[3]

We used the bolometer camera LABOCA (large APEX bolometer camera, Siringo et al. 2009) to observe 94 Cet, project ID 090.F-9302(A). The LABOCA operating wavelength is 870 μm, centred on a 150-μm-wide window. The 295 bolometers yield a circular field

[3] http://www.apex-telescope.org/telescope/

of view of 11.4 arcmin and the beam has a FWHM of 19.5 arcsec. It uses different mapping modes to fill the undersampled parts of the array; we used the on-the-fly mode, in which the maps are scanned back-and-forth linearly row-by-row or column-by-column. Skydips determined the atmospheric opacity with τ values between 0.19 and 0.40, with an average of ∼0.30 and a precipitable water vapour <1 mm.

The observations were centred on the J2000 coordinates RA $3^{h}12^{m}46\overset{s}{.}44$ and Dec. $-1^{\circ}11'46\overset{''}{.}0$ and produced an 11.4 × 12.7 arcmin sized map. Calibrations yield 5.9 ± 0.6 Jy beam^{-1} μV^{-1} with Uranus and Neptune as calibrators.[4] The data were reduced with CRUSH using the deep field setting.[5]

The final reduced image has a pixel resolution of 4 arcsec pixel^{-1} and the flux density is given in Jy beam^{-1}. The flux densities of point sources are measured directly from their peak pixel, and the error estimate is given by the rms of the background around each source, i.e. in a region extending between two beam radii to 60 arcsec from the source.

3.3 Ancillary data

We took optical data from two different sources: Strömgren *uvby* photometry from Hauck & Mermilliod (1997) and Johnson *BV* plus Cousins *I* from Perryman et al. (1997). *JHK*$_s$ Two Micron All Sky Survey (2MASS) data were taken from Cutri et al. (2003). For the mid-IR regime, we took data from the *Wide-field Infrared Survey Explorer* (*WISE*) and the *Akari* satellites; the *WISE* data were taken from the All-Sky Data Release Catalogue (Wright et al. 2010) and the *Akari* data were taken from the *Akari*/IRC mid-IR all-sky survey (Ishihara et al. 2010). We took data from the *Infrared Astronomical Satellite* (*IRAS*) from the *IRAS* Point Source Catalogue (Helou & Walker 1988). Finally, we complemented the SED using *Spitzer* data. *Spitzer*/MIPS (Rieke et al. 2004) observations are published and summarized in more detail by Trilling et al. (2008). A *Spitzer*/IRS (Houck et al. 2004) spectrum (PID 102, PI: Werner, Rebull et al. 2008) extracted from the DUNES data base, and not reprocessed by us, is also shown with the SED.

3.4 Observational results

Since the angular distance between 94 Cet A and BC during the observations was 2.4 arcsec and the 100-μm beam FWHM is 6.8 arcsec, the photometry presented here includes the fluxes from all 94 Cet components.

The photometric data are presented in Table 4 and the stellar SED is presented in Fig. 3. Excesses are clearly detected, both at 100 and 160 μm (12σ and 10σ, respectively), and marginally at 70 μm (3.4σ, where σ denotes the error estimate at each wavelength). The photospheric spectrum was extracted from the high-resolution PHOENIX/GAIA grid (Brott & Hauschildt 2005) by Eiroa et al. (2013) with the parameters summarized in Table 2. For the companion stars, we used synthetic spectra from the PHOENIX library by Husser et al. (2013) (assuming similar metallicities as 94 Cet A, [Fe/H] = 0.2). We approximated the long wavelength part of the spectra (>10 μm for B and C, and >50 μm for A) with Rayleigh–Jeans tails. The spectra were normalized using the *V*-band magnitude 11.5 for 94 Cet B+C and the B and C flux density ratio of 0.29 (Röll et al. 2011, 2012) was used.

Table 4. Summary of photometry used in the analysis of 94 Cet.

$\lambda_{\rm eff}$ (μm)	S_ν (mJy)	Photometry reference
0.349	7943 ± 673	Strömgren *u* (1)
0.411	19850 ± 819	Strömgren *v* (1)
0.440	23410 ± 431	Johnson *B* (2)
0.466	28710 ± 530	Strömgren *b* (1)
0.546	34720 ± 640	Strömgren *y* (1)
0.550	34130 ± 629	Johnson *V* (2)
0.790	42710 ± 787	Cousins *I* (2)
1.235	34110 ± 8895	2MASS *J* (3)
1.662	31850 ± 7038	2MASS *H* (3)
2.159	21120 ± 4628	2MASS K_s (3)
3.353	10560 ± 1159	*WISE* (W1) (4)
9	1645 ± 19	*Akari* (5)
11.561	1001 ± 12	*WISE* (W3) (4)
12	968.8 ± 58.1	*IRAS* (6)
18	427.6 ± 14.2	*Akari* (5)
22.088	289.1 ± 5.3	*WISE* (W4) (4)
24	218.0 ± 4.4	MIPS (7)
25	225.3 ± 42.8	*IRAS* (6)
70	42.50 ± 4.76	MIPS (7)
100	37.85 ± 2.08	PACS (8)
160	24.92 ± 2.08	PACS (8)
100	49.20 ± 3.81[a]	PACS (8)
160	46.46 ± 7.41[a]	PACS (8)
100	38.19 ± 1.75	PACS (9)
160	29.56 ± 1.16	PACS (9)
870	≤9.59 (3σ)	LABOCA (10)

Notes. [a]Total flux density of both central source and extended emission.

References. (1) Hauck & Mermilliod (1997). (2) *Hipparcos* (Perryman et al. 1997). (3) 2MASS Point Source Catalogue (Cutri et al. 2003). (4) *WISE* All-Sky Data Release Catalogue (Wright et al. 2010). (5) *Akari*/IRC mid-IR all-sky survey, II297 in Vizier, colour corrected (Ishihara et al. 2010). (6) *IRAS* Point Source Catalogue, II/125 in Vizier, colour corrected (Helou & Walker 1988). (7) *Spitzer*/MIPS (Trilling et al. 2008). (8) *Herschel*/PACS, this work, colour corrected. (9) *Herschel*/PACS, estimates by Eiroa et al. (2013), colour corrected. (10) APEX-LABOCA, this work.

Our PACS photometry results are similar to those of Eiroa et al. (2013) (colour corrected; 38.19 ± 1.75 mJy at 100 μm and 29.56 ± 1.16 mJy at 160 μm); this is caused by the differences in HIPE versions, in PACS calibration trees and in aperture corrections. Our 100 μm image has a rms between 2.0 and 2.4 mJy beam^{-1} and our 160 μm image has a rms between 3.3 and 4.0 mJy beam^{-1}; they contain some background sources labelled as numbers 1–5 (1–4 are visible in Fig. 4).

The emission that appears around the central source at 100 and 160 μm may be associated with 94 Cet. We estimate the total flux density of the extended source by separating it into eastern, southern and western regions designated simply as E, S and W in Fig. 4. The angular distances, from the observed stellar position, for each of these regions are 18.0 arcsec for east, 17.1 arcsec for south and 35.1 arcsec for west; these correspond to projected distances from the main source of 407, 387 and 794 au, respectively. The eastern

[4] Primary calibrators are Mars, Uranus and Neptune, and secondary calibrators are listed at http://www.apex-telescope.org/bolometer/laboca/calibration/

[5] Comprehensive Reduction Utility for SHARC-2 http://www.submm.caltech.edu/∼sharc/crush/

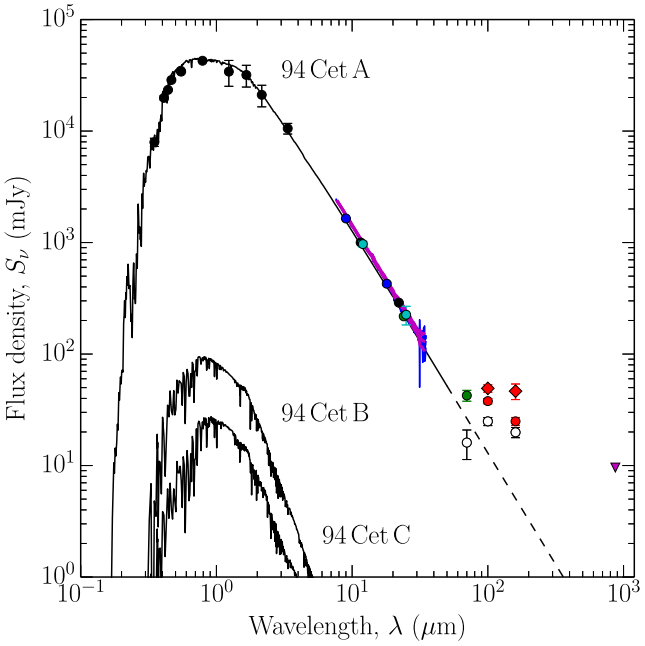

Figure 3. Observed photometry and photospheric model SEDs of 94 Cet A, B and C. The model photospheres are shown as black lines. The dashed line is an extrapolated Rayleigh–Jeans tail of the stellar photosphere from 50 μm, under the assumption of blackbody emission. The plotted photometric data points and 1σ uncertainties are also presented in Table 4 (several error bars are smaller than the data point symbol) and the upper limit (triangle) is a 3σ limit. Black data points are *Hipparcos*, 2MASS, *WISE* and Strömgren data; blue are *Akari*; green are *Spitzer*/MIPS and red are *Herschel*/PACS. The magenta upper limit is from APEX-LABOCA. The magenta and blue spectra denote the *Spitzer*/IRS spectrum, where the magenta spectrum is binned to decrease the noise at 30 μm. The red diamonds represent the combined flux density of the extended emission and the central source, and the empty circles are the excess data (observations subtracted by the photospheric model).

and western extensions are aligned along the projected plane of the companion star's orbit around the primary. The southern extension is along the direction to the companion stars. A close up of the region, including the orbits and stellar positions, are shown in Fig. 5.

To estimate the flux densities for each region, we began by subtracting a standard PACS PSF from the main source, also shown in Fig. 5. This PSF was normalized to the flux density of the nearby point source 94 Cet 2 to avoid underestimating the fluxes by subtracting the extended central emission. The flux densities for each region were then estimated as point sources and the results are presented in Table 5. The total flux density of the whole 94 Cet system is listed in Table 4 and plotted in Fig. 3 as red diamonds.

Among the standard PACS PSFs listed in the *Herschel* technical document PICC-ME-TN-033 (Lutz 2015), we chose α Boötis because it has the highest SNR. Additionally, Kennedy et al. (2012) found that the PSF widths vary about 2–4 per cent at 100 μm and ∼1 per cent at 160 μm, so the effect of choosing another reference star is negligible.

4 SURROUNDING SOURCES

It is imperative that we first distinguish which sources are not part of the 94 Cet system and which are likely part of it. We then focus on the latter and attempt to provide the first constraints on their positions in the system, i.e. if they are due to circumstellar, circumbinary or even circumtertiary dust emission.

4.1 Background contamination

Background confusion is an important issue at 100 and 160 μm. When studying cold circumstellar dust, 100 μm is the preferred wavelength because of its sensitivity to the emission of dust with temperatures of ∼100 K and because of the high contrast between the dust and the host star. However, dust emission from high-redshift galaxies may also have significant flux densities at this wavelength, which could be misinterpreted as part of the disc emission.

Hence, we can estimate the probability of contamination by background galaxies. In fig. 7 of Berta et al. (2011), it is shown that the number of galaxies with a flux density greater than 2 mJy beam^{-1} is about 2–6 × 10^3 deg^{-2}, or 1–3 × 10^{-2} beam^{-1}. This number decreases significantly with increased flux. For example, at 6 mJy beam^{-1} (three times the background rms), the number of expected galaxies decreases to 3–7 × 10^2 deg^{-2}, or 1–3 × 10^{-3} beam^{-1}. For the 94 Cet excess at 100 μm (25 mJy), the number count has dropped to 1–3 × 10^{-4} beam^{-1}; this gives a probability of up to 2.3 per cent of coincidental alignment for a given source at these flux levels. In comparison, our estimated probability is lower than that reported in Krivov et al. (2013), in which they calculated a 4.8 per cent probability of confusion between background galaxies and the coldest debris discs yet found.

As mentioned before, in the PACS image we see a number of background sources (see Appendix). Those with SNR > 3 are listed in Table A1 and those in the LABOCA field are listed in Table A2. Most of the LABOCA sources are positioned outside the PACS field and not visible in Fig. 4.

4.2 Pointing accuracy

The average *Herschel* pointing offset ($\sigma_{\rm point}$) for this observing period (OD 661) is 2.36 arcsec (Sánchez-Portal et al. 2014). The last column in Table 3 refers to the observed offset, i.e. the difference between the observed position and J2000 position compensated for the proper motion of the 94 Cet system.

The observed offsets of 94 Cet are 2.1$\sigma_{\rm point}$ and 2.6$\sigma_{\rm point}$ at 100 and 160 μm, respectively, and while they are marginally significant, there are three scenarios that could explain them. First, the observed emission does not belong to the 94 Cet system and actually originates from a background galaxy but, as we showed earlier, the probability of this is lower than 3 per cent. Secondly, the *Herschel* pointing offset, $\sigma_{\rm point}$, could have been larger for these observations, implying that our observed offsets are smaller and the observed emission actually matches the position of the primary star of the system. Thirdly, the observed emission is actually on the expected position for the BC companion pair and originates from a circumbinary debris disc around them.

The second scenario is weakened by the analysis done in Eiroa et al. (2013), in which they found that the dust emission temperature corresponds to a distance to the primary star where no stable orbits can exist due to influences from the secondary. Meanwhile, the third scenario is strengthened by the orbital measurements from Roberts et al. (2011), which locate the BC companion pair at observed offsets of 1.1$\sigma_{\rm point}$ and 1.6$\sigma_{\rm point}$ for 100 and 160 μm, respectively. As such, we continue with our analysis assuming the third scenario is correct.

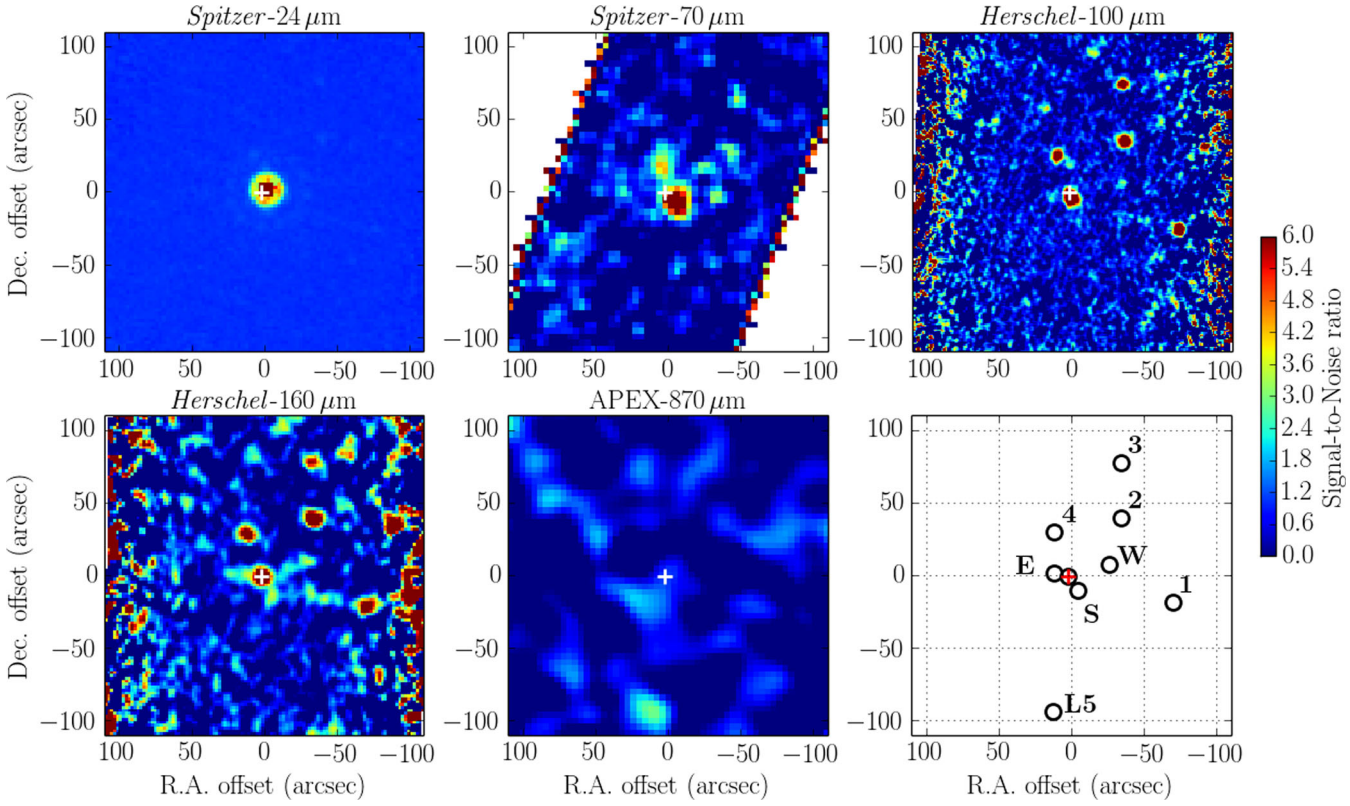

Figure 4. SNR maps of the *Spitzer*/MIPS 24 and 70 μm images (as extracted from the *Spitzer* archive, Trilling et al. 2008), the *Herschel*/PACS 100 and 160 μm images (observed by Eiroa et al. 2013) and our APEX-LABOCA 870 μm observation. The lower right image identifies background sources found in the field, numbered in the same order as in Tables A1 and A2. The stellar position is indicated with a cross, and E, S and W denote the eastern, southern and western extensions (see the text).

5 STABLE ORBITS AND DISC SIZES

Multiple star systems give rise to interesting dynamics. In this system, we can expect stable orbits around each of the stars, circumbinary orbits around the two secondary stars, and circumtertiary orbits around the whole system. Using the semi-analytical expression based on simulations by Holman & Wiegert (1999), we can estimate the sizes of stable regions, expressed as critical semi-major axes, around each star in a binary (see also Wiegert et al. 2014 and references therein).

We proceeded by calculating the critical semi-major axes for 94 Cet B and C independently ($a_{\rm B.crit}$ and $a_{\rm C.crit}$), followed by coupling them and forming the BC binary component ($a_{\rm BC.crit}$). The BC component was then coupled with 94 Cet A to form the A-(BC) tertiary system ($a_{\rm A.crit}$ and $a_{\rm ABC.crit}$, see Fig. 1).

We found the following maximum radii for stable regions in the 94 Cet system, with error estimates in parentheses, and the corresponding angular sizes based on the distance to the system:

$$\begin{cases} a_{\rm A.crit} \approx 47.1 \text{ au (14 per cent)} = 1.8 \text{ arcsec (15 per cent)} \\ a_{\rm B.crit} \approx 0.2 \text{ au (22 per cent)} = 0.009 \text{ arcsec (22 per cent)} \\ a_{\rm C.crit} \approx 0.1 \text{ au (39 per cent)} = 0.004 \text{ arcsec (44 per cent)} \\ a_{\rm BC.crit} \approx 36.4 \text{ au (22 per cent)} = 1.6 \text{ arcsec (23 per cent)}. \end{cases} \quad (1)$$

The fifth critical semi-major axis, i.e. for circumtertiary orbits, can be approximated to be at least three times the semi-major axis (Wiegert & Holman 1997; Holman & Wiegert 1999), which corresponds to $a_{\rm ABC.crit} \sim 660$ au from the system barycentre. The western source is at an angular distance of 35.1 arcsec, which corresponds to 794 au at this distance. Its position angle and distance fit well with a possible circumtertiary dust ring.

Although this disc would extend on scales of several hundreds of astronomical units, its having a collisionally active belt is not excluded. First, significantly extended debris discs have already been observed around solar-like stars, for instance around HD 202628 where the disc extends up to ∼200 au (Krist et al. 2012), HD 207129 with a belt at ∼160 au (Löhne et al. 2012), and ζ^2 Ret (HIP 15371, Faramaz et al. 2014), which has a wide stellar binary companion and a resolved, asymmetric disc at ∼100 au. Secondly, the presence of a massive gravitational perturber, such as the BC pair orbiting the primary, is expected to increase the eccentricities of planetesimals inside the belt and raise the collisional activity, all the more since it is on an eccentric orbit.

Due to its large extent, this system may have suffered from perturbations from Galactic tides and passing stars. Indeed, this type of perturbation is expected to induce pseudo-random losses of angular momentum on bodies orbiting their host star at large separations, whether these bodies are planetesimals (Heisler & Tremaine 1986) or stellar binary companions (Kaib, Raymond & Duncan 2013). Consequently, the orbits of these bodies tend to acquire small pericentres, which for planetesimals will potentially lead to cometary activity (Kaib & Quinn 2009). On the other hand, if it is a stellar binary companion, the survival of material around the primary may be more endangered and the architecture of any planetary system formed may be dramatically reshaped (Kaib et al. 2013). These effects are expected to be significant for old (gigayear) systems and for bodies orbiting at very large separations (between 10^3 and 10^4 au). Since the separations involved for the 94 Cet system are

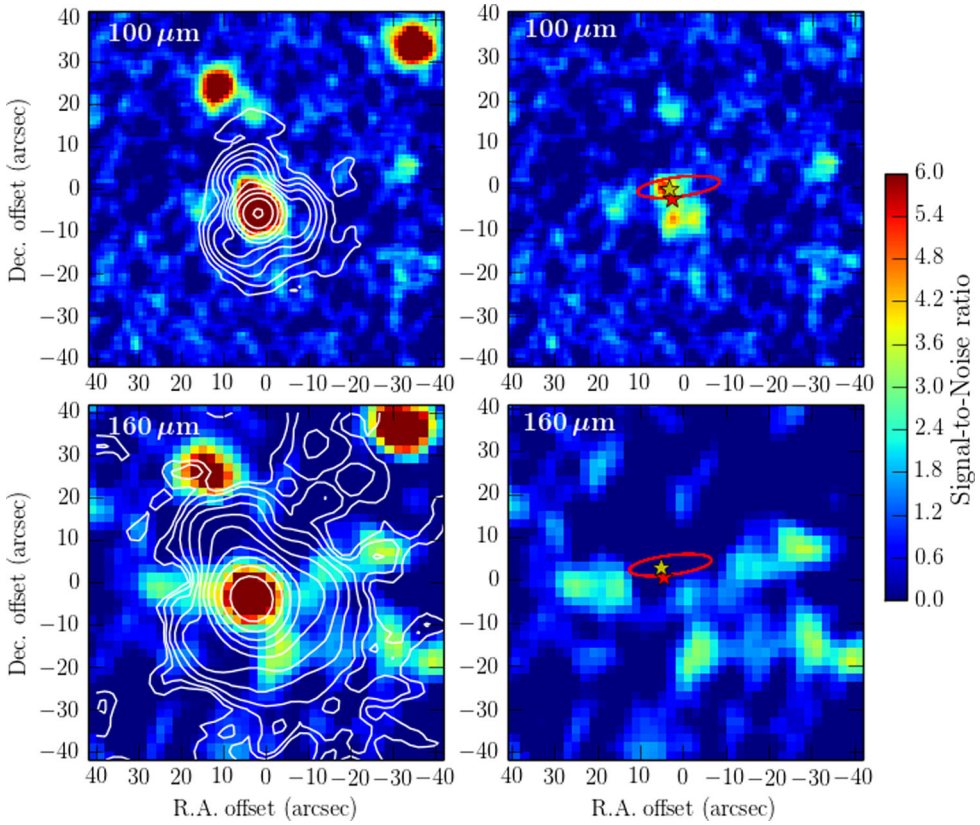

Figure 5. The surrounding area around 94 Cet. Each row is for each PACS wavelength. The first column shows the observations and the contours of the PSF (white) correctly rotated and positioned on the central source. The PSF is shown in logarithmic scale to emphasize the shape and the positions of the tri-lobes. The second column shows the observations when subtracted by PSFs positioned on the sources. The central source was subtracted by a PSF normalized to the flux density of 94 Cet 2. The positions of 94 Cet A (yellow star) and 94 Cet BC (red star), and their orbit (red ellipse) around the primary (based on the parameters in Roberts et al. 2011) are also indicated. 1 arcsec corresponds to ∼23 au.

Table 5. Flux densities of source extensions.

Source	S_ν(100 μm) (mJy)	S_ν(160 μm) (mJy)
Eastern	4.2 ± 0.5	8.5 ± 1.8
Southern	2.7 ± 0.5	5.5 ± 1.2
Western	4.5 ± 0.7	7.6 ± 2.3

smaller than these values, this system is most probably not affected significantly by Galactic tides and passing stars.

As mentioned before, Eiroa et al. (2013), using a blackbody fit, attempted to retrieve the dust location. They found a disc radius of 95 au, far inside the unstable region. Using the comparisons between blackbody radii and resolved radii by Pawellek & Krivov (2015), we finally estimate a range of true radii for this blackbody radius, i.e. 267–455 au when taking error bars into account.

6 NUMERICAL STUDY

The resulting true radii are not sufficiently accurate and, therefore, we resort to full radiative transfer modelling to derive more accurate values. We also use *N*-body symplectic simulations as a complementary approach to our analytical estimates of the locations of stable orbits in this system.

6.1 Radiative transfer modelling

We use the Monte Carlo based program RADMC-3D presented in Dullemond (2012).[6] We use the disc constraints previously derived and combine them with RADMC-3D to obtain simulated SEDs and images of the different disc models. The parameters we used are summarized in Table 6 and described hereafter.

6.1.1 Dust properties

The mass absorption coefficient, $\kappa_{\rm abs}$, describes how well the dust grains absorb and re-emit radiation. We obtained it from the extinction coefficients ($\kappa_{\rm ext}$) of Miyake & Nakagawa (1993), who studied the effects of different grain sizes and size distributions of compact spherical silicate grains. The minimum grain size, which dominates the emission, is assumed to be $\sim\lambda/(2\pi)$. We use the 100-μm data because of its better resolution and we assume minimum observed sizes between 10 and 100 μm. The extinction coefficients are normalized with a gas-to-dust ratio of 100 (see Liseau et al. 2015, and references therein).

We compare these opacities with other more recent studies: Weingartner & Draine (2001), Zubko, Dwek & Arendt (2004) and Draine (2006) for interstellar dust, and Kataoka et al. (2014) for dust aggregates in protoplanetary discs. All these works show mass absorption coefficients between 1 and 10 $\rm cm^2\ g^{-1}$ at wavelengths around

[6] http://www.ita.uni-heidelberg.de/~dullemond/software/radmc-3d/

Table 6. Parameters for RADMC-3D simulations.

Parameter	Value
Grain size range, a (μm)	8 to 10^{3a}
Blow-out radius, $a_{\rm blow\text{-}out}$ (μm)	1.3^{b}
Grain density, ρ (g cm^{-3})	2.5
Size distribution, $n(a) \propto a^{-q}$ (cm^{-3})	$q = 2$ to 4^{c}
Surface density, $\Sigma(r) \propto r^{-\gamma}$ (g cm^{-2})	$\gamma = -2$ to 2
Vertical distribution, $h(r)$ (au)	$0.1 \times r^{d}$
Absorption coefficient, $\kappa_{\rm abs}(a, q, \rho)$ (cm^2 g^{-1})	$\kappa_{\rm ext}(1-\eta)^{e}$
Scatter coefficient, $\kappa_{\rm scat}(a, q, \rho)$ (cm^2 g^{-1})	$\kappa_{\rm ext}\eta^{e}$
Inner disc radius, $r_{\rm in}$ (au)	$r(T_{\rm vap})^{f}$
Outer disc radius, $r_{\rm out}$ (au)	$a_{\rm crit}{}^{g}$

Notes. [a] $a_{\rm min} \approx 6 \times a_{\rm blow\text{-}out}$ (Wyatt, Clarke & Booth 2011; Löhne et al. 2012; Thébault 2016). [b] Plavchan et al. (2009). [c] Dohnanyi (1969). [d] Artymowicz (1997). [e] Miyake & Nakagawa (1993); Inoue et al. (2008). [f] Inner disc radius is limited by vaporization temperature, $T_{\rm vap} = 1800$ to 1300 K (Pollack et al. 1994; Moro-Martin 2013). [g] See equation (1) and dynamical simulations.

300 μm. However, they assume smaller grains than we expect in a circumstellar environment. Grains smaller than 10 μm tend to exhibit up to two orders of magnitude higher absorption at shorter wavelengths (<100 μm) and stronger silicon features than grains of, e.g., 1 mm. The final grain size range and size distribution exponent, q, are also significant contributors to the inferred total dust disc mass. $q = 3.5$ was first suggested by Dohnanyi (1969) but we vary it between 2 and 4 in steps of 0.5.

The lower size limit is based on an inferred blow-out radius of the grains ($a_{\rm blow\text{-}out}$), i.e. the smallest possible grains allowed due to stellar pressure forces (Plavchan et al. 2009; Wiegert et al. 2014). Simulations (Wyatt et al. 2011; Löhne et al. 2012; Thébault 2016) show that the lower cut-off is smooth and a good approximation of the smallest allowed grain size should be around 6 times the blow-out radius. We can compute the blow-out radius by assuming a mass grain density of 2.5 g cm^{-3} and obtain 1.3 μm for 94 Cet A. Kirchschlager & Wolf (2013) found that only stars with effective temperatures higher than 5250 K have a determined blow-out radius and, since the companion stars are of M type with effective temperatures under 4000 K, it is not expected for them to have a blow-out radius. Nevertheless, we assume the much brighter primary star generates a blow-out radius for the complete system. Since the larger grains do not contribute to the thermal emission of the dust, we fix the upper grain size to 1 mm, the same value as several studies, which allows us to have comparable results.

The albedo (η) may vary widely depending on grain constituents and possible ice covering. Miyake & Nakagawa (1993) and Inoue et al. (2008) both studied the albedo of grains with different sizes and with/without ice covering. They showed that the albedo for small silicate particles ($a \lesssim 10$ μm) is relatively stable between 0.5 and 0.6 and then drops down to zero at longer wavelengths between 100 and 500 μm.

We estimate the optical depth at three different wavelengths: 0.5, 100 and 160 μm. We use the chosen extinction coefficients and cloud densities of 10^{-20}–10^{-19} g cm^{-3} to obtain values of 0.3–3 $\times$ 10^{-2} at optical wavelengths and 0.6–1 $\times$ 10^{-3} at the FIR wavelengths. From these values, we assume that the discs are optically thin.

We use RADMC-3D, which simulates the whole wavelength range and takes scattering into account, to simulate the heating processes at optical wavelengths, where the disc is less optically thin than at FIR. With more extreme disc models (e.g. higher densities), it might even be optically thick, and we would risk overestimating the emission at FIR and underestimate the mass if we were not using radiative transfer simulations.

As in Wiegert et al. (2014), we start the simulations with a standard disc using the grain size power-law distribution of index $q = 3.5$ (homogeneously distributed in the disc) and radial disc surface density $\gamma = 1$. Keep in mind that $\gamma < -2$ is in reality a ring at the outer edge of the allowed radius, and $\gamma > 2$ is instead a dust ring just outside the vaporization radius. There were only small differences in the resulting SEDs with γ outside the range of −2 to 2.

The accuracy of each model was inspected by eye and quantified with a reduced χ^2 expressed as $1/N \times \sum_{\nu} \left[(S_{\nu}^{\rm obs} - S_{\nu}^{\rm model})/\sigma\right]^2$, where $S_{\nu}^{\rm obs}$ is the observed flux density, $S_{\nu}^{\rm model}$ is the corresponding model flux density and N is the number of data points computed for each wavelength, that is, at 70, 100 and 160 μm, as this is where the emission was found. Through an iterative process, we explored the parameter space to test the degeneracy of each model.

The dust emission models are quantified by the luminosity ratio between the stellar total luminosity and the dust emission luminosity, i.e. $f_{\rm d} \equiv L_{\rm dust}/L_{\star}$.

6.1.2 *Circumstellar disc SEDs*

The results of the radiative transfer simulations of circumstellar discs are shown in the top panel of Fig. 6. The circumprimary disc and companion star circumstellar discs were simulated separately but are shown together. The models were normalized at the 100-μm flux density.

The radius of the circumprimary disc may be located at up to 54 au. The PACS beam radius at the stellar distance corresponds to 81 and 130 au for 100 and 160 μm, respectively, which implies that the disc would not be resolved. The inner radius was set to 0.1 au. There is a planet at 1.4 au that could form gaps in such a disc; however, the available data are insufficient for this to be visible and the models presented here do not include these effects.

The simulated circumprimary disc is in general too warm to fit the data (average temperatures are around 60 ± 20 K). Rings at the outermost edge of the stable region were too warm.

For the companion pair BC, the small orbit significantly limits the radii of circumstellar discs to less than 0.2 au. The simulated SEDs in the top panel of Fig. 6 (red curves) are based on discs with an inner radius of 0.008 au and outer radii of 0.21 and 0.16 au for 94 Cet B and C, respectively. The circumsecondary dust is too warm to fit the observations, with an average dust temperature of 160 ± 70 K.

6.1.3 *Circumbinary disc SEDs*

The circumbinary disc refers to dust orbiting both the secondary stars, 94 Cet B and C. The radial limits from the companion barycentre are 3 to 40 au (0.1 to 1.8 arcsec, equation 1).

The resulting SEDs from RADMC-3D are shown in the middle panel of Fig. 6. Those with $q = 3.5$ were too warm. Reducing the disc into a ring in the outermost parts of the stable region did not reduce the temperature significantly as this did not increase the average distance to the primary star. However, reducing the number of small grains and increasing the number of large grains, i.e. reducing the size distribution q, significantly cools the disc. Thus, we also show simulated SEDs with $q = 3.0$ and 2.5 in the same figure.

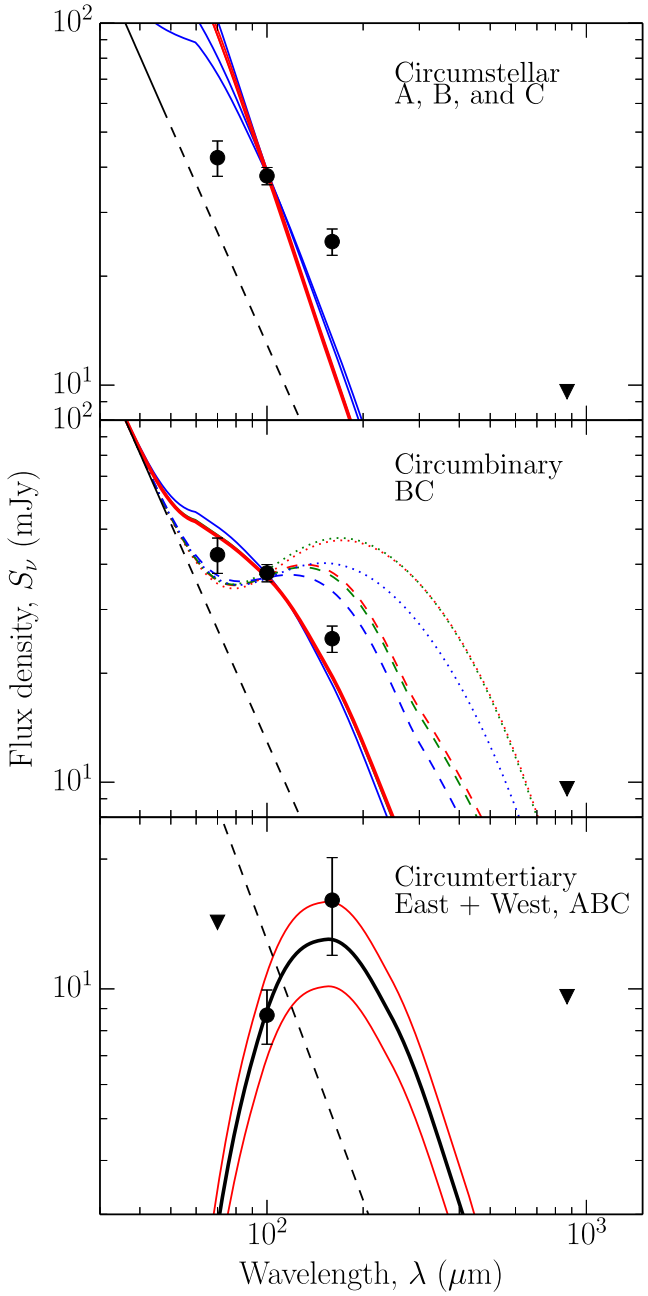

Figure 6. 94 Cet excess models. The thin black line is the model stellar photosphere and the dashed line indicates where a Rayleigh–Jeans tail is assumed. Black dots are photometric data points and the black triangle is a 3σ upper limit. The top panel shows circumstellar discs, both circumprimary (blue) and circumsecondary (red). The middle panel shows circumbinary discs around the secondary pair of stars where the best fit is shown with a thick red line. Models with $\gamma = -2$ are red, $\gamma = 0$ are green and $\gamma = 2$ are blue. $q = 3.5$ is shown with solid lines, $q = 3.0$ with dashed lines and $q = 2.5$ with dotted lines. The lower panel shows the best-fitting circumtertiary dust (black curve) with error estimates as thin red curves, and the data points are the combined flux density of the eastern and western extensions.

The best-fitting dust model ($\chi^2 = 2.6$) corresponds to a disc with $\gamma = -2.0$, $q = 3.5$, average dust temperature of 30.3 ± 7.4 K and a luminosity ratio of $f_\mathrm{d} = 4.6 \pm 0.4 \times 10^{-6}$. The inferred total dust mass would be $6.0 \pm 0.5 \times 10^{-2}\, M_\mathrm{Moon}$. Error estimates are based on an average error of 7.9 per cent of the flux densities at 70, 100 and 160 μm.

A formally better fit could probably be found with q slightly less than 3.5. However, we have too few SED measurements to constrain this better and decrease the χ^2.

6.1.4 *Circumtertiary disc SEDs*

The eastern and western extensions appear where a circumtertiary ring is expected. Fig. 7 compares the observed emission and photometry from a simulated circumtertiary disc at 160 μm based on symplectic particle simulations (see Section 6.2).

We estimate the circumtertiary flux density from the combined fluxes of the eastern and western extensions to 8.7 ± 1.3 mJy at 100 μm and 16.1 ± 4.1 mJy at 160 μm, as plotted in the lower panel of Fig. 6.

Initially, the combined east plus west flux density appears to follow that of a blackbody of a dust ring with a temperature corresponding to the inner dynamical stable radius, 660 au. The emission is, however, unconstrained on the Rayleigh–Jeans part of the SED and a standard dust model with $q = 3.5$ and $\gamma = 1.0$ is sufficient input to RADMC-3D.

The best-fitting model corresponds to a dust ring with fractional luminosity $f_\mathrm{d} \approx 1.4 \pm 0.3 \times 10^{-6}$ and average temperature of 17.0 ± 6.1 K. The temperature is unconstrained though and an upper limit of 30 K is a better estimate. With $q = 3.5$, the total dust mass would be $\sim 0.29 \pm 0.06\, M_\mathrm{Moon}$.

A possible upper limit of the ring radius could, however, be measured directly from the maximum distance between 94 Cet and the outer part of the west extension, i.e. ∼38 arcsec or 860 au.

In Fig. 7, we see that a ring would exhibit peak flux densities at the outer edges to the west and east. This is also where we see the western emission; however, at the eastern edge there is no detectable emission. Furthermore, the eastern extension corresponds better with where the gap would be under the assumption that the ring is in the same orbital plane as the stars. However, an edge-on ring would emit along that region and it may be possible to fit a very clumpy ring.

Another explanation could come from the pericentre glow effect. Pericentre glow appears when a circumstellar ring is eccentric so that the pericentre is more heated than the other parts of the ring, resulting in a horseshoe-shaped source. This effect may occur due to the influence of a companion such as, e.g., a planet (Wyatt et al. 1999; compare with the Fomalhaut ring, Acke et al. 2012).

6.2 *N*-body simulations

Symplectic integration techniques take advantage of the fact that in a planetary system, the mass of the central body is much larger than all the other bodies; however, they fail if all the massive bodies have comparable masses, such as in multiple stellar systems. Therefore, we used the hierarchical Jacobi symplectic (HJS) integrator[7] of Beust (2003), which allows the study of the dynamics of hierarchical stellar systems, provided that the hierarchical structure of the system is preserved along the integration. This code permits us to study the distribution of stable orbits for circumstellar material in this triple star system.

The initial conditions are summarized in Table 7. All simulations contain 10 000 test particles with semi-major axes uniformly

[7] Available at http://ipag.osug.fr/∼beusth/hjs.html

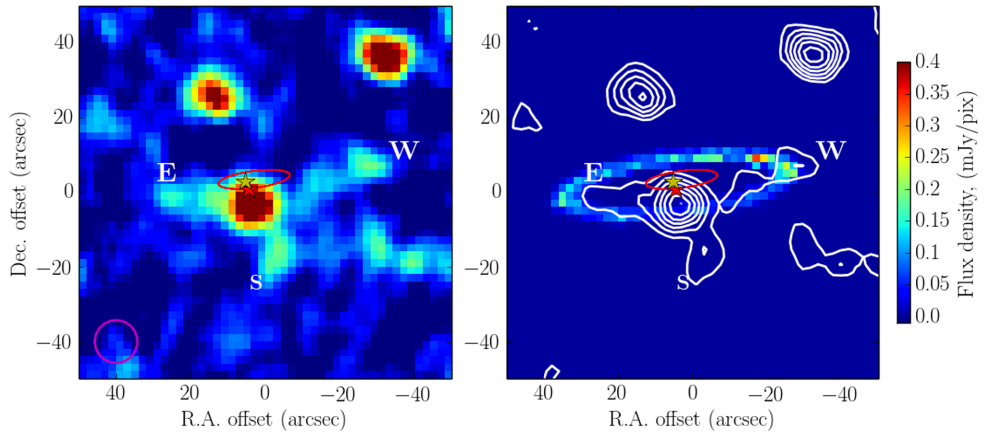

Figure 7. Comparison of observations with circumtertiary ring simulations. The left-hand panel shows the observations at 160 μm with the eastern (E), southern (S) and western (W) extensions, the real position of 94 Cet (yellow and red stars), and the companion pair orbit around the primary (red ellipse). The magenta ring is the observation beam size. The right-hand panel shows the simulated emission of a simulated circumtertiary ring and the 160 μm observation is plotted on top as white contours. The east extension has flux densities 4.2 ± 0.5 mJy at 100 μm and 8.5 ± 1.8 mJy at 160 μm, and the west extension has 4.5 ± 0.7 mJy at 100 μm and 7.6 ± 2.3 mJy at 160 μm.

Table 7. Initial and final conditions of particle disc simulations.

Parameter	Circumprimary	Circumbinary	Circumtertiary
Central star(s)	94 Cet A	94 Cet BC	94 Cet ABC
Initial outer semi-major axis (au)	60	50	750
Final outer semi-major axis (au)	50	40	770
Initial inner semi-major axis (au)	10	3	250
Final inner semi-major axis (au)	10	2.5	590
Number of particles	10^4	10^4	10^4
Length of simulation (Myr)	20	20	20

and randomly distributed between the initial inner and outer values. Their eccentricities are randomly distributed between 0 and 0.05, to mimic the low-eccentricity orbits one can expect at the end of the protoplanetary phase, as well as low inclinations randomly distributed between -3° and 3° relative to the outer orbital plane. The remaining initial angles, longitude of ascending node, longitude of periastron and mean anomaly are randomly distributed between 0 and 2π. We use values corresponding to a cold disc, which is not necessarily true given the age of the system; however, we wish here to test our analytical predictions on the location of stable orbits in the current configuration of the system, so that this simple approach should be sufficient for our purpose.

We ran three separate simulations: circumprimary (around 94 Cet A), circumbinary (around 94 Cet B and C) and circumtertiary. In each case, a time step of 1/20 of the smallest orbital period was used, which ensures the conservation of energy with a typical error of $\sim 10^{-6}$ (Beust 2003). The results are shown in Fig. 8. With a 20 Myr simulation length ($\sim$1/100 of the age of the system), which corresponds to 10 000 orbits of the secondary around the primary, we can assume that the system is stable.

The results are consistent with the estimates in equation (1) (and the discs used for RADMC-3D). The low-density component between 600 and 670 au probably consists of particles in the process of being ejected from the system.

In conclusion, the semi-analytical expression from Holman & Wiegert (1999) is useful also for triple systems where the semi-major axes of the components differ enough so that one can approximate the system as two separate binaries.

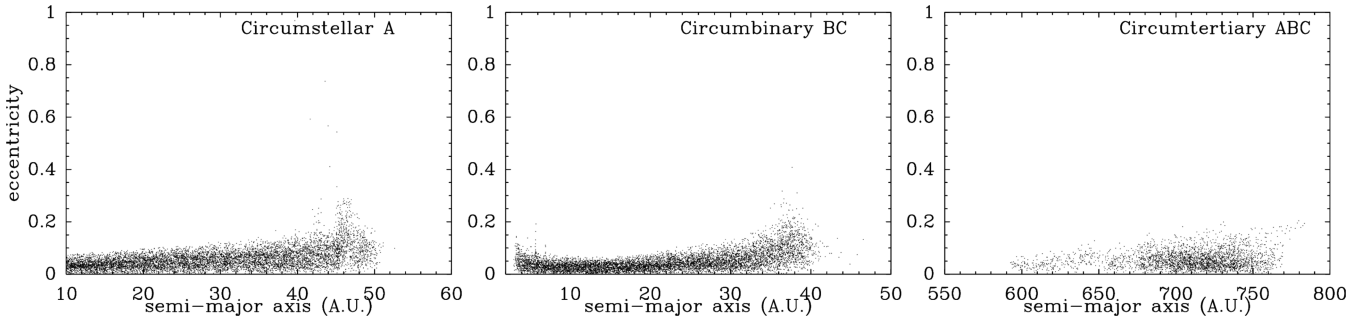

Figure 8. Symplectic particle simulation results. The final eccentricity of each particle orbit is shown against their semi-major axis for circumprimary, circumbinary and circumtertiary discs. Vertical structures appear in the first two panels. The enhancement of the eccentricities of the test particles is due to the orbital eccentricity of the perturbers they are subject to where the disc is truncated. Indeed, for the circumprimary disc, which is under the influence of the pair BC in an eccentric orbit, the enhancement appears at the outer edge of the disc only, while it appears both at the inner and outer edges in the circumbinary case, since the disc is under the influence of the eccentric orbit of C around B at the inner edge, and under the influence of the eccentric orbit of A at the outer edge.

7 CONCLUSIONS

Multi-component systems pose many difficult questions concerning planet formation processes. 94 Cet provides one of the few unique opportunities of a case study of a triple stellar system (Röll et al. 2011, 2012) with at least one planet (Eggenberger et al. 2003) and FIR excess (Trilling et al. 2008; Eiroa et al. 2013). For these reasons and a marginally significant offset in the PACS data, we aimed to model the stellar excess and simulate the orbital dynamics of the system.

(i) The central source fits well with that of a circumbinary disc around the companion pair (inside the dynamically stable radii) at 30.3 ± 7.4 K, with a dust grain size distribution q between 3 and 3.5, and fractional luminosity $f_{\rm d} = 4.6 \pm 0.4 \times 10^{-6}$. The disc extends from 3 to 40 au from the barycentre of the companion stars with a surface density distribution that is $\propto r^2$. Assuming $q = 3.5$ and a grain size range of 8 μm–1 mm, this corresponds to $6.0 \pm 0.5 \times 10^{-2}\, M_{\rm Moon}$.

(ii) The eastern and western extensions have flux densities of 8.7 ± 1.3 mJy at 100 μm and 16.1 ± 4.1 mJy at 160 μm, which correspond well with the possibility of a circumtertiary ring of dust ($q = 3.5$) with the fractional luminosity $f_{\rm d} \approx 1.4 \pm 0.3 \times 10^{-6}$ and temperature of <30 K. However, the uncertainty is significant and the temperature is unconstrained. The ring was assumed to extend from an inner edge at 600–650 to ∼750 au, and the initial surface density distribution $\propto r^{-1}$.

(iii) The system and disc configurations are stable after 20 Myr. The particle discs were simulated with the symplectic integrator HJS (Beust 2003) using 10^4 particles for each disc.

Our models provide evidence for the possibility of both circumsecondary and circumtertiary dust. It is possible that the lack of circumprimary (hotter) dust emission is due to additional planets emptying the circumprimary neighbourhood and our evidence for the circumtertiary ring is only tentative. As such, it would be useful to constrain further the nature of this system through additional observations.

Even without *Herschel*, there are a few possibilities available. ALMA, for example, could probably not observe any circumtertiary dust, but may be able to confirm our findings for the circumsecondary dust, and the Large Millimeter Telescope in Mexico can observe 94 Cet during the autumn and could reach a 3σ of 0.3 mJy in 36 h, possibly enough to reach the dust emission.

ACKNOWLEDGEMENTS

We would like to thank R. Liseau, and also C. Eiroa, G. Kennedy, A. Krivov, J.P. Marshall and K. Torstensson for their many comments, insights and support for this project. We appreciate the continued support of the Swedish National Space Board for our *Herschel* projects. V. Faramaz acknowledges the support from FONDECYT Postdoctoral Fellowships, project 3150106, and the support from the Millenium Nucleus RC130007 (Chilean Ministry of Economy) and Millennium Nucleus 'Protoplanetary Disks'. F. Cruz-Saenz de Miera is supported by CONACyT research grant SEP-2011-169554. Many thanks to Hervé Beust for his guidance using the HJS code.

This research made use of the Exoplanet Orbit Database and the Exoplanet Data Explorer at exoplanets.org; the SIMBAD data base operated at CDS, Strasbourg, France; 2MASS, which is a joint project of the University of Massachusetts and the Infrared Processing and Analysis Center/California Institute of Technology and funded by the National Aeronautics and Space Administration (NASA) and the National Science Foundation; and the NASA/IPAC Extragalactic Database, which is operated by the Jet Propulsion Laboratory, California Institute of Technology, under contract with the National Aeronautics and Space Administration.

REFERENCES

Acke B. et al., 2012, A&A, 540, A125
Andrews S. M., Czekala I., Wilner D. J., Espaillat C., Dullemond C. P., Hughes A. M., 2010, ApJ, 710, 462
Apai D., Schneider G., Grady C. A., Wyatt M. C., Lagrange A.-M., Kuchner M. J., Stark C. J., Lubow S. H., 2015, ApJ, 800, 136
Artymowicz P., 1997, Annu. Rev. Earth Planet. Sci., 25, 175
Artymowicz P., Lubow S. H., 1994, ApJ, 421, 651
Aumann H. H., 1985, PASP, 97, 885
Balog Z. et al., 2014, Exp. Astron., 37, 129
Bergfors C. et al., 2013, MNRAS, 428, 182
Berta S. et al., 2011, A&A, 532, A49
Bessell M. S., 1991, AJ, 101, 662
Beust H., 2003, A&A, 400, 1129
Beust H. et al., 2014, A&A, 561, A43
Booth M. et al., 2016, MNRAS
Brott I., Hauschildt P. H., 2005, in Turon C., O'Flaherty K. S., Perryman M. A. C., eds, ESA Special Publ. Ser. Vol. 576, The Three-Dimensional Universe with Gaia. ESA, Noordwijk, p. 565
Cataldi G., Brandeker A., Olofsson G., Chen C. H., Dent W. R. F., Kamp I., Roberge A., Vandenbussche B., 2015, A&A, 574, L1
Chary R., Elbaz D., 2001, ApJ, 556, 562
Cieza L. A. et al., 2009, ApJ, 696, L84
Contro B., Wittenmyer R. A., Horner J., Marshall J. P., 2015, in Origins of Life and Education of Biospheres, Vol. 45. Springer Netherlands, Dordrecht, p. 41
Cox A. N., 2000, Allen's Astrophysical Quantities. Springer, New York
Cutri R. M. et al., 2003, VizieR Online Data Catalog, 2246
Daemgen S., Hormuth F., Brandner W., Bergfors C., Janson M., Hippler S., Henning T., 2009, A&A, 498, 567
Dent W. R. F. et al., 2014, Science, 343, 1490
Desidera S., Barbieri M., 2007, A&A, 462, 345
Dodson-Robinson S. E., Beichman C. A., Carpenter J. M., Bryden G., 2011, AJ, 141, 11
Dohnanyi J. S., 1969, J. Geophys. Res., 74, 2531
Draine B. T., 2006, ApJ, 636, 1114
Duchêne G., 2010, ApJ, 709, L114
Duchêne G., Kraus A., 2013, ARA&A, 51, 269
Dullemond C. P., 2012, RADMC-3D: A multi-purpose radiative transfer tool (ascl:1202.015)
Duquennoy A., Mayor M., 1991, A&A, 248, 485
Eggenberger A., Udry S., Mayor M., 2003, in Deming D., Seager S., eds, ASP Conf. Ser. Vol. 294, Scientific Frontiers in Research on Extrasolar Planets. Astron. Soc. Pac., San Francisco, pp. 43–46.
Eggenberger A., Udry S., Chauvin G., Beuzit J.-L., Lagrange A.-M., Ségransan D., Mayor M., 2007, A&A, 474, 273
Eggleton P. P., Tokovinin A. A., 2008, MNRAS, 389, 869
Eiroa C. et al., 2013, A&A, 555, A11
Elbaz D. et al., 2011, A&A, 533, A119
Elbaz D. et al., 2013, VizieR Online Data Catalog, 353, 39119
Faramaz V. et al., 2014, A&A, 563, A72
Faramaz V., Beust H., Augereau J.-C., Kalas P., Graham J. R., 2015, A&A, 573, A87
Fuhrmann K., 2008, MNRAS, 384, 173
Gomes R., Levison H. F., Tsiganis K., Morbidelli A., 2005, Nature, 435, 466
Hale A., 1994, AJ, 107, 306
Harris R. J., Andrews S. M., Wilner D. J., Kraus A. L., 2012, ApJ, 751, 115
Hauck B., Mermilliod M., 1997, VizieR Online Data Catalog, 2215, 0

Heisler J., Tremaine S., 1986, Icarus, 65, 13
Helou G., Walker D. W. eds 1988, Infrared Astronomical Satellite (IRAS) Catalogs and Atlases Vol. 7, NASA, Washington, DC
Helou G., Madore B. F., Schmitz M., Bicay M. D., Wu X., Bennett J., 1991, in Albrecht M. A., Egret D., eds, Astrophysics and Space Science Library Vol. 171, Databases and On-line Data in Astronomy. Springer Netherlands, Dordrecht, p. 89
Holman M. J., Wiegert P. A., 1999, AJ, 117, 621
Houck J. R. et al., 2004, ApJS, 154, 18
Husser T.-O., Wende-von Berg S., Dreizler S., Homeier D., Reiners A., Barman T., Hauschildt P. H., 2013, A&A, 553, A6
Inoue A. K., Honda M., Nakamoto T., Oka A., 2008, PASJ, 60, 557
Ishihara D. et al., 2010, A&A, 514, A1
Jang-Condell H., 2015, ApJ, 799, 147
Jang-Condell H., Mugrauer M., Schmidt T., 2008, ApJ, 683, L191
Kaib N. A., Quinn T., 2009, Science, 325, 1234
Kaib N. A., Raymond S. N., Duncan M., 2013, Nature, 493, 381
Kalas P. et al., 2008, Science, 322, 1345
Kataoka A., Okuzumi S., Tanaka H., Nomura H., 2014, A&A, 568, A42
Kennedy G. M., Wyatt M. C., Sibthorpe B., Phillips N. M., Matthews B. C., Greaves J. S., 2012, MNRAS, 426, 2115
Kirchschlager F., Wolf S., 2013, A&A, 552, A54
Kóspál Á., Ardila D. R., Moór A., Ábrahám P., 2009, ApJ, 700, L73
Kraus A. L., Ireland M. J., Hillenbrand L. A., Martinache F., 2012, ApJ, 745, 19
Krist J. E., Stapelfeldt K. R., Bryden G., Plavchan P., 2012, AJ, 144, 45
Krivov A. V., Müller S., Löhne T., Mutschke H., 2008, ApJ, 687, 608
Krivov A. V. et al., 2013, ApJ, 772, 32
Lada C. J., 2006, ApJ, 640, L63
Lawler S. M. et al., 2014, MNRAS, 444, 2665
Lawler S. M., Greenstreet S., Gladman B., 2015, ApJ, 802, L20
Lim J., Takakuwa S., 2006, ApJ, 653, 425
Liseau R. et al., 2015, A&A, 578, A131
Löhne T. et al., 2012, A&A, 537, A110
Lutz D., 2015, PACS Photometer Point Spread Function, PICC-ME-TN-033, v. 2.2. Available at: http://herschel.esac.esa.int/twiki/pub/Public/PacsCalibrationWeb/bolopsf_22.pdf
Mamajek E. E. et al., 2013, AJ, 146, 154
Marshall J. P. et al., 2014, A&A, 565, A15
Mayor M., Udry S., Naef D., Pepe F., Queloz D., Santos N. C., Burnet M., 2004, A&A, 415, 391
Millar-Blanchaer M. A. et al., 2015, ApJ, 811, 18
Miyake K., Nakagawa Y., 1993, Icarus, 106, 20
Montesinos B. et al., 2016, A&A, preprint (arXiv:1605.05837)
Moore A., Quillen A. C., 2013, MNRAS, 430, 320
Moro-Martin A., 2013, in Oswalt T. D., French L. M., Kalas P., eds, Planets, Stars, and Stellar Systems. Springer Netherlands, Dordrecht, p. 431
Mugrauer M., Neuhäuser R., Seifahrt A., Mazeh T., Guenther E., 2005, A&A, 440, 1051
Müller T. G., Okumura K., Klaas U., 2011, PACS Photometer Passbands and Colour Correction Factors for Various Source SEDs, PICC-ME-TN-038, v. 1.0. Available at: http://herschel.esac.esa.int/twiki/pub/Public/PacsCalibrationWeb/cc_report_v1.pdf
Muterspaugh M. W. et al., 2010, AJ, 140, 1657
Nesvold E. R., Kuchner M. J., 2015, ApJ, 815, 61
Ott S., 2010, in Mizumoto Y., Morita K.-I., Ohishi M., eds, ASP Conf. Ser. Vol. 434, Astronomical Data Analysis Software and Systems XIX. Astron. Soc. Pac., San Francisco, p. 139 (arXiv:1011.1209)
Pawellek N., Krivov A. V., 2015, MNRAS, 454, 3207
Payne M. J., Ford E. B., Wyatt M. C., Booth M., 2009, MNRAS, 393, 1219
Perryman M. A. C. et al., 1997, A&A, 323
Pilbratt G. L. et al., 2010, A&A, 518, L1
Plavchan P., Werner M. W., Chen C. H., Stapelfeldt K. R., Su K. Y. L., Stauffer J. R., Song I., 2009, ApJ, 698, 1068
Poglitsch A. et al., 2010, A&A, 518, L2
Pollack J. B., Hollenbach D., Beckwith S., Simonelli D. P., Roush T., Fong W., 1994, ApJ, 421, 615
Queloz D., Mayor M., Naef D., Pepe F., Santos N. C., Udry S., Burnet M., 2004, in Penny A., Artymowicz P., Lagrange A. M., Russel S., eds, IAU Symp. Vol. 202, Planetary Systems in the Universe. Manchester, p. 106
Quintana E. V., Adams F. C., Lissauer J. J., Chambers J. E., 2007, ApJ, 660, 807
Rafikov R. R., Silsbee K., 2015, ApJ, 798, 69
Raghavan D., Henry T. J., Mason B. D., Subasavage J. P., Jao W.-C., Beaulieu T. D., Hambly N. C., 2006, ApJ, 646, 523
Raghavan D. et al., 2010, ApJS, 190, 1
Rajpurohit A. S., Reylé C., Allard F., Homeier D., Schultheis M., Bessell M. S., Robin A. C., 2013, A&A, 556, A15
Rebull L. M. et al., 2008, ApJ, 681, 1484
Reid I. N. et al., 1991, PASP, 103, 661
Rein H., 2012, preprint (arXiv:1211.7121)
Rieke G. H. et al., 2004, ApJS, 154, 25
Rigby E. E. et al., 2011, MNRAS, 415, 2336
Riviere-Marichalar P. et al., 2014, A&A, 565, A68
Roberts L. C., Jr, Turner N. H., ten Brummelaar T. A., Mason B. D., Hartkopf W. I., 2011, AJ, 142, 175
Rodriguez D. R., Duchêne G., Tom H., Kennedy G. M., Matthews B., Greaves J., Butner H., 2015, MNRAS, 449, 3160
Röll T., Seifahrt A., Neuhäuser R., Köhler R., Bean J., 2011, in Turon C., Meynadier F., Arenou F., eds, EAS Publ. Ser., GAIA: At the Frontiers of Astrometry. EDP Sciences, London, p. 429
Röll T., Neuhäuser R., Seifahrt A., Mugrauer M., 2012, A&A, 542, A92
Saffe C., Gómez M., 2004, A&A, 423, 221
Sánchez-Portal M. et al., 2014, Exp. Astron., 37, 453
Siringo G. et al., 2009, A&A, 497, 945
Skrutskie M. F. et al., 2006, AJ, 131, 1163
Smyth W. H., 1844, A Cycle of Celestial Objects. J. W. Parker, London
Su K. Y. L., Rieke G. H., Defrére D., Wang K.-S., Lai S.-P., Wilner D. J., van Lieshout R., Lee C.-F., 2016, ApJ, 818, 45
Thébault P., 2016, A&A, 587, A88
Thébault P., Marzari F., Scholl H., 2009, MNRAS, 393, L21
Trilling D. E. et al., 2007, ApJ, 658, 1264
Trilling D. E. et al., 2008, ApJ, 674, 1086
Weingartner J. C., Draine B. T., 2001, ApJ, 548, 296
Wiegert P. A., Holman M. J., 1997, AJ, 113, 1445
Wiegert J. et al., 2014, A&A, 563, A102
Wright E. L. et al., 2010, AJ, 140, 1868
Wu X., Roby T., Ly L., 2010, in Mizumoto Y., Morita K.-I., Ohishi M., eds, ASP Conf. Ser. Vol. 434, Astronomical Data Analysis Software and Systems XIX. Astron. Soc. Pac., San Francisco, p. 14
Wyatt M. C., 2008, ARA&A, 46, 339
Wyatt M. C., Dermott S. F., Telesco C. M., Fisher R. S., Grogan K., Holmes E. K., Piña R. K., 1999, ApJ, 527, 918
Wyatt M. C., Clarke C. J., Booth M., 2011, Celest. Mech. Dynamical Astron., 111, 1
Zubko V., Dwek E., Arendt R. G., 2004, ApJS, 152, 211

APPENDIX: BACKGROUND GALAXIES

We list background sources found in the PACS fields and LABOCA field in Tables A1 and A2.

Five background sources with SNR > 3 were found in the PACS field. For the positions of the sources 94 Cet 2 and 5, we found the catalogued sources SSTSL2 J031244.01-011111.8 and SSTSL2 J031248.04-010850.9, respectively, in the *Spitzer* Heritage Archive.[8] However, they were not found in other large catalogues (e.g. 2MASS,[1] Skrutskie et al. 2006 or NASA/IPAC Extragalactic

[8] Searched through the NASA/IPAC Infrared Science Archive, Caltech/JPL (https://irsa.ipac.caltech.edu/, Wu, Roby & Ly 2010).

Table A1. PACS-field background sources, coordinates and spectral indices with wavelengths 160 and 870 μm.

Source	RA (J2000) h m s	Dec. (J2000) ° ′ ″	Spectral index,[a] α
94 Cet[b]	3 12 46.43	−1 11 51.8	≤0.56
94 Cet 1	3 12 41.56	−1 12 12.6	≤0.51
94 Cet 2[c]	3 12 44.02	−1 11 12.5	≤0.64
94 Cet 3	3 12 44.08	−1 10 33.5	≤0.43
94 Cet 4	3 12 47.08	−1 11 22.8	≤0.38
94 Cet 5[d]	3 12 48.05	−1 08 51.1	≤0.77
Average index of background			≤0.64

[a]Spectral index for $\lambda = 870$ and 160 μm, and defined as $S_\nu \propto \nu^\alpha$. [b]Observed coordinates, not from references. [c]Coordinates correspond with SSTSL2 J031244.01-011111.8. [d]Coordinates correspond with SSTSL2 J031248.04-010850.9.

Table A2. LABOCA-field background sources, coordinates, and flux densities.

Source	RA (J2000) h m s	Dec. (J2000) ° ′ ″	S_ν (mJy)
94 Cet L1	3 12 39.08	−1 17 06.8	18.70 ± 5.93
94 Cet L2	3 12 42.30	−1 15 32.2	14.55 ± 3.73
94 Cet L3	3 12 46.02	−1 16 16.3	16.13 ± 4.81
94 Cet L4	3 12 46.56	−1 07 00.0	16.56 ± 5.49
94 Cet L5	3 12 47.37	−1 13 20.3	14.62 ± 2.73
94 Cet L6	3 12 51.89	−1 09 36.0	17.97 ± 4.11
94 Cet L7	3 12 58.34	−1 13 02.5	16.05 ± 3.90

Database[9]). They were not visible in the Palomar Sky Survey (Reid et al. 1991), possibly due to the large PSF of the star in IR. However, in the MIPS 24-μm data, we notice weak sources (i.e. SNR < 3) at the positions of the PACS background sources, and that 94 Cet 4 coincides with a ring feature (a beam artefact) that appears around the source at 24 μm.

The field appears to lack previously detected sources. There are, however, a great number of sources to the west of the field. The lack of catalogued sources is not surprising though, as the stars in the DUNES catalogue were deliberately chosen to avoid regions of noisy background, such as, e.g. the Galactic plane. In the POSS IR images, 94 Cet 3 possibly appears, however, very weakly. The other sources are either covered by the large PSF from the star or too faint. We do see the sources denoted as 94 Cet 2, 3 and 4 in the MIPS 70-μm data; however, all of these have SNR < 3. As mentioned, the stellar proper motion between *Spitzer* and *Herschel* observations are just slightly more than 1 arcsec.

In Table A1, we clearly see that all sources have similar upper limit spectral indices (upper limits due to non-detections in the LABOCA data) as the central source. We also compare these data with larger samples of FIR galaxies from GOODS-*Herschel* (Elbaz et al. 2011, 2013) and *Herschel*-ATLAS (Rigby et al. 2011) in Fig. A1. We define the spectral index α as $S_\nu \propto \nu^\alpha$ with wavelengths from $\lambda = 160$ to 350, 500 or 870 μm depending on available data.

[9] The NASA/IPAC Extragalactic Database is operated by the Jet Propulsion Laboratory, California Institute of Technology, under contract with NASA (http://ned.ipac.caltech.edu/, Helou et al. 1991).

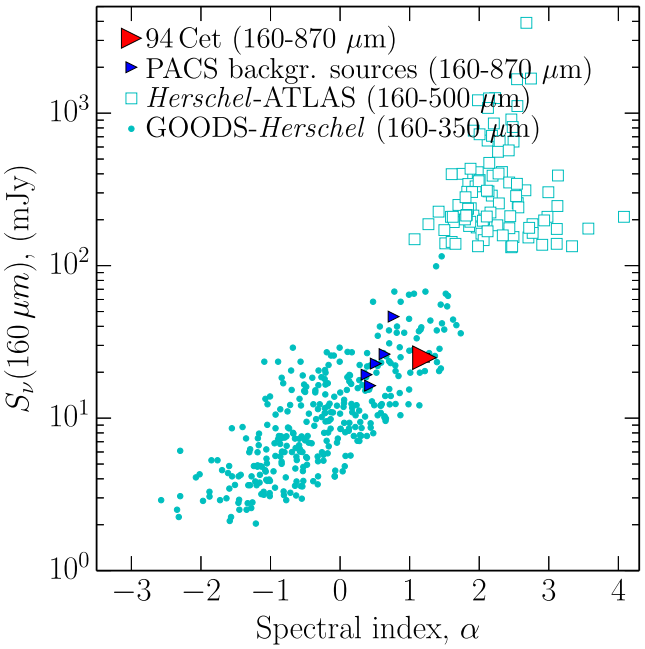

Figure A1. Spectral index map of the sources listed in Table A1 and FIR galaxies. Cyan dots are spectral indices of FIR galaxies from the north field of the GOODS-*Herschel* (Elbaz et al. 2011, 2013) with $\lambda = 160$ to 350 and 500 μm. Cyan squares are spectral indices of FIR galaxies from *Herschel*-ATLAS (Rigby et al. 2011) with $\lambda = 160$ to 500 μm. The red triangles indicate the 94 Cet upper limit spectral index (using 1σ upper limit at 870 μm), and the blue triangles are background sources upper limits with $\lambda = 160$ to 870 μm (3σ upper limit at 870 μm).

However, we also see that it is difficult to distinguish the stellar excess from the background sources and other FIR galaxies by looking at the spectral indices. This is not strange as we are comparing extragalactic dust with circumstellar dust at these wavelengths.

The similarities are clearer if we compare with model SEDs of FIR galaxies (red-shifts of $z \sim 0.2$ to 2) from Chary & Elbaz (2001).[10] These show that FIR galaxies tend to have peak flux densities at PACS wavelengths while at optical and near-IR wavelengths, the flux densities are significantly lower. If we compare with 2MASS completeness limits, we see that not even the most extreme galaxies (with the highest star-forming rates) at red shifts higher than 0.5 should be detectable at optical or near-IR wavelengths.

Most of the PACS background sources are likely FIR galaxies. However, the central source is extended in nature and fits the positions and position angles of the stellar components, its orbit and the expected size of a circumtertiary ring. With a 2 per cent probability of coincidental alignment, we find it very improbable that the dust emission seen at 94 Cet could be attributed to a FIR background galaxy.

[10] Templates and instructions are available at http://david.elbaz3.free.fr/astro_codes/chary_elbaz.html.

This paper has been typeset from a TEX/LATEX file prepared by the author.